

PCCP

Accepted Manuscript



This is an *Accepted Manuscript*, which has been through the Royal Society of Chemistry peer review process and has been accepted for publication.

Accepted Manuscripts are published online shortly after acceptance, before technical editing, formatting and proof reading. Using this free service, authors can make their results available to the community, in citable form, before we publish the edited article. We will replace this *Accepted Manuscript* with the edited and formatted *Advance Article* as soon as it is available.

You can find more information about *Accepted Manuscripts* in the [Information for Authors](#).

Please note that technical editing may introduce minor changes to the text and/or graphics, which may alter content. The journal's standard [Terms & Conditions](#) and the [Ethical guidelines](#) still apply. In no event shall the Royal Society of Chemistry be held responsible for any errors or omissions in this *Accepted Manuscript* or any consequences arising from the use of any information it contains.

Theoretical vibrational spectra of $\text{OH}^-(\text{H}_2\text{O})_2$: Effect of quantum distribution and vibrational coupling

Yudai Ogata¹, Yukio Kawashima², Kaito Takahashi^{*3}, and Masanori Tachikawa^{**1}

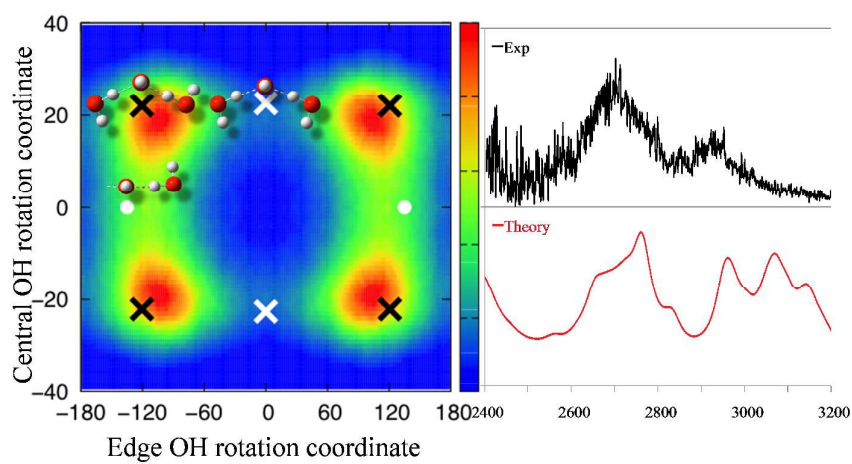
¹ *Graduate school of Nanobioscience, Yokohama City University, Yokohama 236-0027, Japan*

² *RIKEN Advanced Institute for Computational Science, Kobe 650-0047, Japan*

³ *Institute of Atomic and Molecular Sciences, Academia Sinica, P.O. Box 23-166, Taipei 10617, Taiwan, Republic of China*

*Corresponding author: kt@gate.sinica.edu.tw

**Corresponding author: tachi@yokohama-cu.ac.jp

Graphical abstract

Quantum distribution of $\text{OH}(\text{H}_2\text{O})_2$ and the vibrational spectra computed using these geometries.

Abstract

We performed *ab initio* path integral molecular dynamics simulations for hydroxide-water cluster $\text{OH}^-(\text{H}_2\text{O})_2$ at 50 K, 100 K, and 150 K to investigate its flexible structure. From our simulations, we found that nuclear quantum effects enhance hydroxide hydrogen atom inversion and the conformational change between isomers occurs by simultaneous rotation of the free hydrogen atom. We propose the importance of including the transition state conformer with C_2 symmetry, for the description of this system at temperatures realized in predissociation experiments. Temperature dependence on relative populations of each conformer along with multidimensional vibrational calculation were used to simulate the vibrational spectra and compared with the experimental spectra of Johnson and coworkers. We assign the doublet peaks seen in the experiment at 2500 to 3000 cm^{-1} , as the mixture of ionic hydrogen bonded OH stretching overtone, ionic hydrogen bonded OH bending overtone, and the combination band of the ionic hydrogen bonded OH stretch and bend, which are modulated by the van der Waals OO vibrations. We concluded that for $\text{OH}^-(\text{H}_2\text{O})_2$, the vibrational couplings between the ionic hydrogen bonded motion and floppy modes contribute to the broadening of peaks observed in the 2500 to 3000 cm^{-1} region.

Keywords: anion water cluster; hydroxide ion; nuclear quantum effect; path integral molecular dynamics; ionic hydrogen bond; vibrational spectra;

1. Introduction

Hydroxide ion has an essential role in aqueous chemistry [1-16]. It is well known that hydroxide ion forms anion water cluster, $\text{OH}^-(\text{H}_2\text{O})_n$, with n water molecules in aqueous environment. In these clusters, ionic hydrogen bonds (IHBs) are formed between the oxygen of hydroxide ion and the hydrogen of the water molecules. IHB is extremely strong compared to usual hydrogen bonds, therefore there are some difficulties in analyzing detailed structures of IHB due to its large flexibility and its large anharmonicity.

For $\text{OH}^-(\text{H}_2\text{O})_n$ ($n = 1\sim 5$) Johnson and co-workers reported vibrational spectra for these clusters at low temperature using Ar-tagging techniques [5]. The experimental vibrational spectra have shown that the hydroxide ion directly binds to three water molecules as the first solvent shell. Furthermore, they reported assignments of the spectra with comparison to harmonic normal mode calculations for the most stable conformers of $\text{OH}^-(\text{H}_2\text{O})_{1-5}$. The fundamentals of IHB OH stretching vibration were assigned to the experimental peaks at 2700 cm^{-1} , 2600 cm^{-1} , and 2900 cm^{-1} for $\text{OH}^-(\text{H}_2\text{O})_2$, $\text{OH}^-(\text{H}_2\text{O})_3$, and $\text{OH}^-(\text{H}_2\text{O})_4$ clusters, respectively. However, from the perspective of chemical bond strength, the hydrogen bonds should be strengthened with decreasing number of directly bonded water molecules, i.e. the IHB peak positions should be red shifted with decreasing number of water molecules. Nevertheless, the peak positions are blue shifted from $\text{OH}^-(\text{H}_2\text{O})_3$ to $\text{OH}^-(\text{H}_2\text{O})_2$ in experimental spectra.

To understand this inconsistency, one of the authors previously reported theoretical vibrational spectra with multidimensional local mode calculations evaluated by the second-order Møller-Plesset perturbation theory (MP2) for the two stable

conformers: Conformer I and II of $\text{OH}^-(\text{H}_2\text{O})_2$ shown in Figure 1 [11]. Furthermore, they also simulated the thermal averaged spectra by combining the spectra of two stable conformers. In their previous study, electronic energies and the respective vibrational frequencies were used to estimate the free energies of the two stable isomers. They assigned the experimental peak at 2700 cm^{-1} as the overtone of IHB OH stretching vibration and mentioned that the fundamental should be located around $1600\sim 1900\text{ cm}^{-1}$. These results are consistent with the point of view of the systematic increase in hydrogen bond strength with decrease in the number of water molecules n . On the other hand, the theoretical simulation did not fully reproduce the experimental spectrum, and the theoretical peak positions showed blue shifts of $\sim 300\text{ cm}^{-1}$ from the experimental spectra. In the present study we approach this system from two different directions to remedy this discrepancy. First, only stable minima conformers were used for the calculations of spectra, and the populations of the stable conformers were decided fairly roughly. Second, the treatment of just the local OH stretching vibration may have been incomplete for the proper description of the vibrational spectra at the 2000 to 3000 cm^{-1} region for the very anharmonic $\text{OH}^-(\text{H}_2\text{O})_2$.

In our previous studies, it was found that both thermal and nuclear quantum effects are indispensable to describe the detailed geometrical distributions of small ion water clusters such as $\text{OH}^-(\text{H}_2\text{O})_n$ formed by IHB [16-19]. In fact, the experimental structure for $\text{OH}^-(\text{H}_2\text{O})$ and theoretical one without thermal and nuclear quantum effects are qualitatively different. The experimental structure is reproduced theoretically by including both effects. Furthermore, we previously reported the nuclear quantum and thermal effects on the hydrogen bond structures of $\text{OH}^-(\text{H}_2\text{O})_2$ at 300 K , and found that the two hydrogen-bonded protons come close to central hydroxide ion by including nuclear quantum and thermal effects [19], i.e. the $\text{OH}^- \cdots \text{H}^+ \cdots \text{OH}^- \cdots \text{HOH}$ or

HOH...OH⁻...H⁺...OH⁻ like structures exist. However, we note that both protons never simultaneously approach the central hydroxide, and the OH⁻...H⁺...OH⁻...H⁺...OH⁻ like structure was not found.

Therefore, in this paper, we investigate nuclear quantum and thermal contributions to carefully derive the existence ratio of the conformers. For this purpose, we carry out *on-the-fly ab initio* path integral molecular dynamics (PIMD) [15-23] simulations for OH⁻(H₂O)₂ and analyze the detailed conformation and these existence ratios with thermal and nuclear quantum effects at low temperatures. Here, we mainly discuss the orientation of the free hydrogen atoms, H2, H4, and H5 shown in Figure 1. We consider the thermal effect on OH⁻(H₂O)₂ at the temperature of experimental condition. The experimental temperature is speculated to be extremely low but it is very hard to experimentally quantify, therefore we used the temperature range of 50-150 K, which has been mentioned in previous experimental studies [11, 24]. In addition, we simulated the vibrational spectra using the distributions obtained from the present PIMD studies and compared them with the spectra simulations obtained from the static calculations.

Furthermore, several of our previous studies were performed based on the assumption that the OH stretching vibrational modes dominate the spectra. However, recent studies on hydrated clusters have mentioned the importance of the coupling of the hydrogen bonded OH stretching mode to the low frequency intermolecular modes such as water wagging, water rotation, and van der Waals (VDW) water-water stretching modes.[25-27] Thereby in the present study we performed vibrational calculation including the anharmonic coupling of the IHB OH stretching modes to the IBH OH bending, and VDW stretching modes.

The rest of the paper is organized in the following manner. In section 2, the details for the path integral methods as well as vibrational calculation will be given. In section 3, we present the detailed analysis of the simulated population as well as a comparison of the theoretical vibrational spectra with the previous experiments by Johnson and coworkers. Lastly we provide a brief conclusion in section 4.

2. Computational details

2.1 Path integral simulation

We carried out *ab initio* PIMD simulations [16-20], later denoted as quantum simulation, for $\text{OH}^-(\text{H}_2\text{O})_2$. Here, all oxygen and hydrogen atoms were treated as quantum mechanical particles by bead expansion based on the path integral method. Quantum simulation was performed for 200,000 steps with 96 beads, 48 beads, and 32 beads for 50 K, 100 K, and 150 K after a thermal equilibration of 5,000 steps using time step size of 0.1 fs. Furthermore, we also performed the conventional *ab initio* molecular dynamics simulations, later denoted as classical simulation, to elucidate the nuclear quantum effect, where all nuclei are treated as classical particles. Classical simulations were performed 2,000,000 steps with 1 bead for 50 K, 100 K, and 150 K after a thermal equilibration of 20,000 steps using time step size of 0.1 fs. All electronic structure calculations in the quantum and classical simulations were performed by B3LYP functional [28, 29] with the resolution of identity approximation [30, 31] using TZVP basis set (RI-B3LYP/TZVP) in TURBOMOLE package [32]. Quantum and classical simulations were performed at 50 K, 100 K, and 150 K with massive Nosé-Hoover chain thermostat [33] to achieve canonical ensemble in the same manner as in our previous works [16-20]. Figure 1 shows the schematic illustrations of $\text{OH}^-(\text{H}_2\text{O})_2$

optimized by the conventional electronic structure calculations, with atomic numberings used in this paper.

2.2 Multidimensional vibrational calculation

There are some difficulties in obtaining vibrational spectra of $\text{OH}^-(\text{H}_2\text{O})_n$, which include IHB with large geometrical flexibility and anharmonicity. So, harmonic normal mode (NM) calculations may not provide quantitative spectra for floppy $\text{OH}^-(\text{H}_2\text{O})_2$. Hence, we initially carried out multidimensional local mode calculation for $\text{OH}^-(\text{H}_2\text{O})_2$ concentrating only on the OH stretching vibrations. However, we noticed that similar to previous studies the peak position was blue shifted from the experiment by $\sim 300 \text{ cm}^{-1}$, so instead of using only the OH stretching internal coordinates, we performed reduced dimensional vibrational calculation using selected NM's. As shown in Figure 2 for Conformer I, in addition to the two IHB OH stretching modes (2(a)/(b)), we considered the two IHB bending modes (2(c)/(d)), as well as two VDW OO stretching modes (2(e)/(f)), which are mixed with the hydroxide rocking motion. For the free OH and hydroxide stretching vibrations (See Figure S1 in the electronic supplementary material), we performed a 3 dimensional coupled calculation. Thus the spectra is obtained from the summation of the IHB stretching part, which we performed 2D, 4D, or 6D simulations, with the 3D simulation for the other 3 OH vibrations. In the NM picture the kinetic energy has no couplings and the Hamiltonian is written as

$$\sum_{i=1}^n -\frac{\hbar^2}{2m_i} \frac{\partial^2}{\partial Q_i^2} + V(Q_1, Q_2, \dots, Q_n),$$

where Q_i and m_i are the NM coordinate and the mass for mode i , respectively. Gaussian 09 [34] package was employed for these calculations, and the NM coordinates were extracted from the Gaussian09 output using the freq=hpmodes keyword. Similar to

previous studies [11, 35], the discrete variable representation with the harmonic oscillator basis was utilized in this study. We used 7 grid points for each degree of freedom, except for the two VDW stretching modes, in which we used 10, thus for the NM6D simulation we performed 2.4×10^5 single point calculations. The potential energy and dipole moments required on the grid points were obtained from single point calculation using MP2/6-311++G(3df,3pd). See ESI for further details concerning the vibrational calculation. We also performed vibrational perturbation theory calculation of Barone and coworkers [36] using the “freq=anharmonic” keyword in Gaussian 09 program [34]. The center of mass was used for the origin of the dipole moment in these anion clusters. To model the spectra we used a homogeneous width of 100 cm^{-1} for peaks below 2250 cm^{-1} ; width of 25 cm^{-1} for peaks above 2250 cm^{-1} and below 3500 cm^{-1} ; and width of 5 cm^{-1} for the free and hydroxide OH peaks. When simulating the spectra we did not consider hot band contribution since the VDW stretching vibrational excited state population was estimated to be $\sim 6\%$.

3. Results and discussion

3.1 Assessments of the calculation level

We first assess our quantum chemistry calculation level for the *on-the-fly* PIMD simulations. Relative energies between two stable conformers and geometrical parameters of $\text{OH}^-(\text{H}_2\text{O})_2$ obtained from several methods are shown in Table 1. We defined the distances between O1/O2 and O3 atoms as $R_{\text{O1O3/O2O3}}$, the relative positions of H1 and H3 atoms as $\delta_{\text{H1/H3}} = R_{\text{O1H1/O2H3}} - R_{\text{O3H1/O3H3}}$, the H2O1O3O2, H4O2O3O1, H2O1O2H4, and H5O1O2O3 dihedral angles as ϕ_1 , ϕ_2 , ϕ_3 , and ϕ_4 , respectively. Schematic images of these dihedral angles are shown in Figure 1.

We optimized the geometries with RI-B3LYP/TZVP, MP2/6-311++G(3df,3pd), and RI-MP2/TZVPP. Furthermore, CCSD(T)/6-311++G(3df,3pd) single point energies at the MP2/6-311++G(3df,3pd) optimized geometry is also obtained. The structural parameters of these optimized structures are presented in Table 1. Similar to our previous study Conformer I is more stable compared to Conformer II in all the calculation levels [11]. The relative energy of Conformer II at MP2/6-311++G(3df,3pd) level is 0.25 kcal/mol (0.04 kcal/mol with zero point energy (ZPE) correction), which is in excellent agreement to the CCSD(T)/6-311++G(3df,3pd) result of 0.26 kcal/mol. In the previous study, MP2/6-311++G(3df,3pd) level was used for geometry optimization and vibrational calculation. So, here, we assumed MP2/6-311++G(3df,3pd) level as the reference value.

In our PIMD scheme, both energies and forces are obtained from the *on-the-fly* electronic structure calculation, therefore calculation using the MP2 method is beyond the capacity of our computational resources. In this sense, we have to assess a computational method that reproduces the reference MP2/6-311++G(3df,3pd) value with reasonable computational cost. The relative energy at RI-B3LYP/TZVP level of theory is 0.28 kcal/mol (0.11 kcal/mol with ZPE correction), while the relative energy at RI-MP2/TZVPP level of theory is 0.36 kcal/mol (0.27 kcal/mol with ZPE correction). From these results, RI-B3LYP/TZVP level of theory fits this criteria in terms of energetics.

Next we focus on the optimized geometries obtained from several levels of theories. The geometries of Conformer I and II optimized by MP2/6-311++G(3df,3pd) level are similar to the other two levels. Among them, RI-B3LYP level has a better agreement, especially in the four dihedral angles. From these results, we selected RI-

B3LYP/TZVP level for our *ab initio* PIMD simulations, which is consistent with our previous study on 300 K [19].

3.2 Hydrogen bond structures

Nuclear quantum and thermal effects on hydrogen bond structures are commonly discussed in many path integral studies [4, 13-20, 37]. According to the custom, we discuss the hydrogen bond structures obtained from classical and quantum simulations as a first step of our analysis. We show average values of $R_{\text{Free OH}}^{\text{Ave.}} = (R_{\text{O1H2}} + R_{\text{O2H4}})/2$, $R_{\text{OO}}^{\text{Ave.}} = (R_{\text{O1O3}} + R_{\text{O2O3}})/2$, R_{O3H3} , and $\delta_{\text{H}}^{\text{Ave.}} = (\delta_{\text{H1}} + \delta_{\text{H3}})/2$, and these standard deviation in Table 2. Here, the statistical errors of average values are also shown in parentheses [38].

For $R_{\text{Free OH}}^{\text{Ave.}}$, the average value of quantum simulation is elongated by 0.015 Å compared to that of classical simulation at all temperatures. This is because quantum simulation includes nuclear quantum effects under the anharmonic potential. Furthermore, the standard deviation value of the quantum simulation is five times larger than that of classical simulation at 50 K. This corresponds to the delocalization of the hydrogen-bonded proton. Also, the standard deviations of quantum simulation do not depend on the temperature, while those of the classical simulation become larger with increasing temperature. The standard deviation for the classical simulation comes from the thermal fluctuation, which, as expected, will increase with temperature. On the other hand, for the quantum simulation, both thermal fluctuation and quantum delocalization of the wavefunction contribute, and here the thermal fluctuation is washed out by the very large quantum delocalization, which does not have much temperature dependence. Thus we found that temperature dependence on hydrogen bond is quite small in

quantum simulation compared to classical simulation. We also saw similar tendency for the hydroxide OH, $R_{O_3H_5}$.

For $R_{OO}^{Ave.}$, the average value of quantum simulation is smaller than that of classical simulation. However, thermal dependence on the peak position is quite small (less than 0.004 Å) in both simulations. Standard deviations in quantum simulations are similar for all temperatures, while that in classical simulations at 150 K becomes dramatically large compared to that at 50 K, i.e. only the distributions in classical simulation broaden by including thermal effect. This feature is similar to $R_{Free\ OH}^{Ave.}$ and $R_{O_3H_5}$.

For $\delta_H^{Ave.}$, the average values of both quantum and classical simulations are negative at all temperatures. This indicates that the hydrogen-bonded proton is localized near the oxygen atom in each water molecule. The protons in quantum simulations are located closer to the center between the hydrogen-bonded oxygen atoms compared to those in classical simulations and static calculations. It is noted that the both protons do not simultaneously approach the center as reported in ref. [19]. Additionally, the temperature dependence on the standard deviations in quantum simulation is smaller than that in classical simulation. Therefore, the proton is more delocalized due to nuclear quantum effects in quantum simulation at 50 K. All these tendencies seen in above are similar to our previous result at 300 K [19].

3.3 Orientations of free hydrogen atoms

The most remarkable difference between the two stable conformers, Conformers I and II, is the orientations of free hydrogen atoms (H2 and H4) at both ends. To analyze the populations of these stable conformers, we introduce two dihedral angles ϕ_1 and ϕ_2 , and plot the two-dimensional distributions of these two variables at each temperature in

Figure 3.

First, we discuss the relative stabilities of the two stable conformers at 50 K where the nuclear quantum effect, the difference between quantum and classical simulations, is most enhanced. From Figure 3(a) and (d), the distributions around the angle that corresponds to Conformer I are relatively large in both classical and quantum simulations. On the other hand, the distributions around Conformer II are extremely small in the classical simulation, while there are ample distributions of Conformer II in the quantum simulation. Furthermore, investigating the temperature dependence, the distributions are delocalized with increasing temperature in both classical and quantum simulations, i.e. the distributions of Conformer I become smaller and those of Conformer II become larger at 150 K compared to 50 K. Moreover, in the quantum simulation at 150 K, we find that the distributions delocalize greatly in the ϕ_1 and ϕ_2 space. The quantitative populations of each conformer will be discussed in the next section.

Next we focus on the qualitative difference in the overall distributions obtained from the classical and quantum simulations at 50 K. In the classical simulation given in Figure 3 (a), a U shaped distributions is seen between two Conformer I isomers (i.e. between two black crosses). There are large distributions at $\phi_1 = \pm 40^\circ$ and $\phi_2 = \pm 40^\circ$, and no distribution at $\phi_1 = \pm 60^\circ$ and $\phi_2 = \pm 60^\circ$ which directly connects the two isomers. The distribution suggests that the conformation change between Conformer I undergo a stepwise process. On the other hand, in the quantum simulation given in Figure 3 (d), the shape of the distribution is linear, i.e. there are large distributions at $\phi_1 = \pm 60^\circ$ and $\phi_2 = \pm 60^\circ$. This indicates that the concerted conformation change is dominant due to quantum tunneling or the rocking motion of the hydroxide as mentioned in the latter sections. As the temperature increases, the

difference between quantum and classical simulations becomes smaller, which is due to the fact that at high temperature, thermal fluctuation in the classical simulation becomes close to the quantum delocalization for this low frequency motion. Schematic images of stepwise and concerted processes of the conformation change discussed here are shown in Figure S2 of the electronic supplementary material.

3.4 Quantum enhancement of free hydrogen atom inversion

As stated above, the orientations of two free OHs obtained from classical and quantum simulations are quite different. Here, we focus on the orientation of the hydroxide hydrogen, H5, and its correlations with the hydrogen on the water molecules. To analyze relative orientation between H2/H4 atom versus H5 atom, we newly introduce two dihedral angles ϕ_3 and ϕ_4 , and plot the two-dimensional distributions of these two variables in Figure 4. Figures 4(a)-(c) illustrate the results from the classical simulations, and (d)-(f) from the quantum simulations. Black and white crosses mark the equilibrium values of Conformer I and II, as in Figure 2.

First, we discuss the one-dimensional distribution along ϕ_4 to simplify the problem. In the classical simulation at 50 K in Figure 3(a), distributions are localized around $\phi_4 \approx \pm 20^\circ$. Meanwhile, in the quantum simulation at 50 K shown in Figure 4(d), distributions are more delocalized and dense population is found at $\phi_4 = 0$, which signify the H5 atom is in the plane defined by O1O3O2 atoms. The motion along ϕ_4 is the H5 atom inversion against the O1O3O2 plane. The distribution of quantum simulation indicates the quantum enhancement of the H5 atom inversion or hydroxide rocking motion at 50 K, while H5 atom is localized on one side in classical simulation.

It is noted that H5 atom inversion can be observed in the classical simulations at higher temperature due to thermal fluctuation, while this is not the case for quantum simulation.

Similar to H2 and H4 atoms, the orientation of H5 atom is significantly different between classical and quantum simulations, therefore, the relationships between H2, H4, and H5 atoms should also show different trends. So, we next discuss the correlation between ϕ_3 and ϕ_4 . In the quantum simulation at 50 K shown in Figure 4(d), there are distributions at $\phi_3 = \pm 120^\circ$, for a wide region of ϕ_4 between $\pm 20^\circ$. Here we note that structures with $\phi_3 = \pm 120^\circ$ corresponds to structures with $\phi_1 = \pm 60^\circ$ and $\phi_2 = \pm 60^\circ$, and correlates with the large distribution at these angles in Figure 3(d). Thus, the qualitative difference of the shape of distribution between classical and quantum simulations shown in Figures 3(a) and (d) is attributed to the quantum enhancement of hydroxide rocking motion. As conclusion, this simulation emphasizes the existence of a new conformer with $\phi_3 = \pm 120^\circ$ and $\phi_4 = 0^\circ$ with C_2 point group symmetry. This C_2 Conformer, given in Figure 4(g), is a transition state with respect to H2, H4, and H5 atoms concerted inversions in static electronic structure calculations. Relative energy of Conformer C_2 from Conformer I is lower (0.11 kcal/mol) than that of Conformer II (0.28 kcal/mol). Hence, while Conformer C_2 is a transition state structure, Conformer C_2 has large distributions compared to Conformer II in quantum simulation at 50 K because inclusion of nuclear quantum effect enhances the H5 atom inversion and overcomes the barrier. On the other hand, in the classical simulation, the inversion of H5 atom is not found under thermal fluctuation of 50 K (≈ 0.1 kcal/mol). The distributions of Conformer II and C_2 completely vanish in classical simulation. That is why the distributions in classical simulation at 50 K shown in Figure 4(a) are localized only around Conformer I.

Furthermore, investigating the temperature dependence, given in Figures 4(a)-(c), the distributions at $\phi_3 = \pm 120^\circ$ and $\phi_4 = 0^\circ$ increase with increasing temperature. This means the H5 atom inversion is found at high temperature in the classical simulations. On the other hand, from Figures 4(d)-(f), the distributions of Conformer C_2 in quantum simulations are not enhanced by thermal fluctuation, and rather the distribution around Conformer II increases. Therefore, in the quantum simulations, the thermal fluctuation contributes to the proton transfer with respect to the rotations of H2 and H4 atoms and delocalization of H2 and H4 atoms rather than H5 atom inversion.

As discussed above, we found that a new conformer, which is a transition state in the static electronic structure calculations, has large populations by carrying out *ab initio* PIMD simulations including both thermal and nuclear quantum effects. To analyze the populations of each conformer quantitatively, the existence ratios were calculated from Figure 4. Here, we defined that the distribution region of Conformers I, II, and C_2 as $|\phi_3| > 60^\circ$ and $|\phi_4| > 15^\circ$; $|\phi_3| < 60^\circ$ and $|\phi_4| > 15^\circ$; and $|\phi_3| \geq 60^\circ$ and $|\phi_4| \leq 15^\circ$, respectively. In addition, for the region, $|\phi_3| < 60^\circ$ and $|\phi_4| < 15^\circ$; we define the region that $4 \times \phi_4 \geq \phi_3$, and $4 \times \phi_4 < \phi_3$ as belonging to conformer II, and C_2 , respectively. Schematic image of these definitions is shown in Figure S3 of the electronic supplementary material. The populations of each conformer obtained from classical and quantum simulations at 50 K, 100 K, and 150 K are shown in Table 3. As given in the electronic supplementary material we have confirmed that the general trend of the obtained population is not sensitive to the definition of the distribution region of the conformers. In conventional calculations like our previous studies, it is customary to perform free energy calculations of the local minimum structures with the rigid rotor harmonic vibration model and obtain the population of these isomers and add up the spectra with their respective populations. So we also

perform similar free energy calculation for each local minimum structure and obtain the population of these conformers at each temperature. Here, the static populations are evaluated by the following equation with the difference of the Gibbs free energy (ΔG) of stable Conformers I and II,

$$\Delta G = -RT \ln\left(\frac{1-x}{x}\right),$$

where R , T , and x denote gas constant, temperature, and relative population of a stable conformer, respectively. We note that only Conformers I and II are used for the static population, and Conformer C_2 is not used because Conformer C_2 is transition state at the static level. Furthermore, the existence ratios for Conformers I and II obtained from free energy calculations with the rigid rotor harmonic vibration model, are weighted by 2:1 due to the degeneracy of the geometrical symmetry.

First, we focus on the populations at 50 K. In classical simulation, Conformer I is dominant with 92.6 %, and other conformers can be negligible. On the other hand, in the quantum simulation, the population of Conformer I is not as large compared to classical simulation with 49.0 %, while Conformer C_2 is comparable to Conformer I with 39.0 %. Similar to the classical simulation, the population of Conformer II is small in the quantum simulation. On the other hand, in the static calculation, the population of Conformer II has a fairly large 30.0 % contribution compared to Conformer I. Thus the static electronic structure calculation overestimates the population of Conformer II compared to quantum and classical simulations at 50 K.

Next, we discuss the thermal dependence on the populations of conformers. The population of Conformer I decreases with the increase in temperature in both classical and quantum simulations. On the other hand, the population of Conformer II is increased in both simulations. This is because the molecular motion is enhanced by thermal fluctuation. However, while the population of Conformer C_2 in quantum

simulation decreases, that in classical simulation increases due to the delocalization of distributions by the increasing of thermal fluctuation. Thus, at 150 K, the C_2 populations in classical and quantum simulations are almost the same. The thermal dependence of the static populations is qualitatively similar to quantum and classical simulations, i.e. the population of Conformer I decreases while that of Conformer II increases with temperature. However, the population of Conformer II is still overestimated at 100 K and 150 K. In the next section, we quantify the effects of this population difference toward the vibrational spectra.

3.5 Effect of mode coupling in the vibrational spectra

In our previous work [11], the vibrational spectra for Conformers I and II of $\text{OH}^-(\text{H}_2\text{O})_2$ were calculated by the multidimensional local mode model and added them with respect to the population ratio. We used a population ratio of 2:1 between Conformers I and II from symmetry of the geometries. In the present work, we explicitly obtained the existence ratios of the conformers using the results of quantum PIMD simulations at several low temperatures. From our simulations, we found that the value of the ratio vastly differs from the previous ratio of 2:1. So, we present the calculated vibrational spectra of Conformers I, II, and C_2 and the thermal averages at 50 K, 100 K, and 150 K in Figure 5.

First, we examine the variation in the spectra for Conformer I following the inclusion of different vibrational modes. As given in Figure 5(a), if we only consider the two IHB OH stretching modes (green color), the IHB OH stretching overtone ($\Delta v=2$) peaks are calculated around 3000 and 3300 cm^{-1} . Similar to the previous local mode simulations [11], the present NM calculations are also found to be blue shifted by $\sim 300 \text{ cm}^{-1}$ compared to the experimental results by Johnson and coworkers [5]. Therefore,

this confirms that the error is not coming from the use of local mode or normal mode representation for the IHB stretching modes.

Due to the strong IHB interaction the fundamental peak for this IHB OH stretching vibration is calculated to be around 1800 and 2000 cm^{-1} . Since these peak positions are close to the IHB OH bending (Figure 3(c)/(d)) fundamental bands, we can imagine a strong mode coupling between them. Indeed the addition of the bending modes (blue lines in Figure 5(a)) causes the two peaks to red shift by $\sim 100 \text{ cm}^{-1}$. This mixing between the IHB OH stretching $\nu=2$ state and the IHB bending $\nu=2$ state allows the simulation results to become closer to the experimental peak positions. Next the addition of the VDW OO stretching modes (red lines in Figure 5(a)) cause further splitting of the two peaks, now resulting in ~ 3 broad peaks in the range of 2500 to 3200 cm^{-1} . In Table 4, we present the selected peak position and intensity calculated by the harmonic approximation, NM4D and NM6D model for conformer I that were used to make these figures. Comparing the harmonic results with the NM4D results, one can clearly notice that due to the strong red shifting of the IHB stretching modes, the bending modes gain intensity through vibrational coupling. Furthermore, in the NM6D calculation, the combination bands at 2312 and 2331 cm^{-1} borrow intensity from the strong IHB stretching band, therefore the large intensity of the IHB stretching band is redistributed around a large frequency region contributing to the broadening of the spectra. Similar broadening and red shift of the spectra are also observed for conformer II and C_2 (see Figure S5 in the electronic supplementary material). This is consistent with recent works on $\text{H}_3\text{O}^+(\text{H}_2\text{O})_3\text{Cl}^-$ [27]. Just like the present case, Mancini and Bowman mentioned that strong coupling of the stretching mode with other modes makes many combination bands and overtone bands in the vicinity of IHB OH stretching peak "borrow" intensity from the strong IHB OH stretching band. Thereby,

making a simple assignment of “pure” fundamental or overtone is very hard. This is also observed in the experimental spectra where one sees a broad peak with width of $\sim 100\text{ cm}^{-1}$ at $2500\text{-}3000\text{ cm}^{-1}$, while the peaks at $\sim 3700\text{ cm}^{-1}$ are very sharp. As conclusion using the 6D NM vibrational calculation, we obtain a spectra where the fundamental, $\Delta v=1$, IHB stretching and IHB bending bands overlap in the region between $1500\text{-}2200\text{ cm}^{-1}$, and their overtones, $\Delta v=2$, overlap in the region $2500\text{-}3000\text{ cm}^{-1}$. In addition, the combination band with VDW OO stretching modes also shows up as humps in 2400 and 3200 cm^{-1} .

3.6 Vibrational spectra including populations

Lastly, we present the 50 K spectra in Figure 5(b) calculated using three different population schemes. For the vibrational spectra, we are not able to see clear differences between the more expensive quantum simulations (red line) versus the simple and easy static simulations (green line). We think this is due to the fact that the general features of the vibrational spectra of the different isomers become similar when we perform vibrational calculation including many couplings in the NM6D model. However one can notice that the QM results are converging toward two main peaks, while in the classical and static simulations we clearly see three peaks. We note that this shape of the spectra does depend on the width used for the simulation, but the general picture stays the same with other combinations of widths. In Figure 5(c) we present the evolution of the 50 K vibrational spectrum with increasing the vibrational degrees of freedom. One can clearly see the red shifting and broadening of the IHB OH stretching peaks. In the experimental spectrum by Johnson *et al.* [5], a clear doublet peak is observed at 2600 to 3000 cm^{-1} . This double peak was previously assigned as the overtone of IHB OH stretching vibration. Following the discussion above and Figure 5(c), we now assign the peaks as the mixture of IHB OH stretching overtone, IHB

bending overtone, and the combination band of the IHB OH stretching and IHB bending, which are modulated with the VDW OO vibrations. Also we note that for the spectra calculated using the 6D NM model we were not able to see clear temperature dependence as given in Figure S6 of the electronic supplementary material.

As seen above, inclusion of the mode coupling and population obtained by the PIMD method have shown improvement in reproducing the experimental spectra, however there are still some discrepancies such as the difference in the intensity ratio between the two humps between 2500-3200 cm^{-1} . Here, we consider the origins of the difference between experimental and theoretical spectra.

In the present study we obtained the population from PIMD simulation or static approximation assuming thermal equilibrium, but as mentioned in previous studies on neutral [39] and protonated water clusters [40], this may not be true. However, if this is the case, we do not have any means to determine the population of the isomers. Methods mentioned by Dieterich and Hartke [39] in optimizing the fit between the experimental results and the simulated spectra of different isomers to determine the population in the experiment condition, may be an answer to this problem.

Next, there is a limitation in the accuracy in the electronic structure method used for the vibrational calculations. To test this, we performed simulation using CCSD(T) energies with the MP2 NM for the 4D model. As can be seen in Figure S7 of the electronic supplementary material, the calculation with CCSD(T) does not show much difference compared to the MP2 results. Thus we believe that limitation in the quantum chemistry is not the likely reason for the discrepancy.

Another reason for the difference can be traced to the effect from the messenger. Ar-tagging used in the experiment can either modulate the population, or modify the vibrational spectra of each conformer. In fact, previous theoretical calculations have

shown that the spectra is red shifted by including argon atom for $\text{OH}^-(\text{H}_2\text{O})_2$ cluster [11]. This kind of modulation of the IHB spectra by messenger tagging has been seen for $\text{H}^+(\text{CO}_2)_n$ and $\text{CH}_3\text{OHH}^+\text{OHCH}_3$ [41, 42]. It will be interesting to see how the Ar-tagging can modify the coupling between the IHB OH stretching modes, and the other modes considered in the study.

Finally, as can be seen from the drastic change in the spectra with the inclusion of mode coupling (see Figure 5(a)/(c)), we expect addition of other modes such as IHB out of plane bending, VDW bending, or low frequency free OH torsion modes may cause further variation in the spectra. In the 50 K PIMD simulation in addition to the hydroxide rocking motion, we noticed that the OOO bending motion was excited more greatly compared to the classical results. Therefore, detailed analysis of the PIMD simulation should be performed to understand the motions that could show up as variations in the observed spectral region. We note that the vibrational perturbation theory calculation, which includes all couplings up to the fourth order, fails for this largely anharmonic system as can be seen in Figure S8 in the electronic supplementary material. Namely, the fundamental peak of the symmetric and asymmetric IHB OH stretching peaks of Conformer I are calculated at 2317 and 1608 cm^{-1} , and the overtones are predicted to be at 3020 and 2869 cm^{-1} . Therefore, perturbation theory is not able to predict the peaks in the region of 2500 to 3000 cm^{-1} . Thus, inclusion of the strongly coupled vibrational degree of freedom in variational manner should be required, and we are presently developing an efficient calculation algorithm to include more vibrational degree of freedoms.

4. Conclusion

We carried out *ab initio* PIMD simulations for $\text{OH}^-(\text{H}_2\text{O})_2$ at 50 K, 100 K, and 150 K

including nuclear quantum and thermal effects to analyse the detailed structures and the existence ratios of conformers. From our simulations, we found that the conformer population is qualitatively different between quantum PIMD, classical molecular dynamics, and statistical simulations. Through these studies we showed the quantum enhancement of hydroxide rock motion in low temperatures. Furthermore, by carrying out PIMD simulations, we showed large population for the Conformer C_2 . This conformer was ignored previously since it was a transition state in static electronic structure calculations. From detailed 6D normal mode vibrational calculation for $\text{OH}^-(\text{H}_2\text{O})_2$, we showed that the coupling between IHB OH stretching and IHB bending motion as well as VDW OO stretching motion can greatly complicate the spectra in the 2500 to 3000 cm^{-1} region. Using these vibrational calculation results and the population of the three conformers, we were able to obtain simulated spectra that qualitatively reproduce the experimental spectra by Johnson et al. For the broad IHB stretching region of 2500 to 3000 cm^{-1} , the subtle differences in the population with the quantum, classical and statistical methods were washed out by the overlapping peaks for the “mixed” vibrational modes in that region. We note that the differences in the population are more apparent in the fundamental peaks positions, 1500-2000 cm^{-1} , therefore future experiments in the low wavenumber region may help gain further understanding on the population distribution of $\text{OH}^-(\text{H}_2\text{O})_2$.

Acknowledgement

Financial support was provided by Grant-in-Aid for Scientific Research and for the priority area by Ministry of Education, Culture, Sports, Science and Technology, Japan for YK and MT. KT thanks Academia Sinica, National Center for High Performance Computing of Taiwan and Ministry of Science and Technology (NSC 102-2113-M-001

-012 -MY3) of Taiwan for support. Theoretical calculations were partly performed at the Research Center for Computational Science, Institute for Molecular Science, Japan.

Reference

1. G. A. Jeffrey, *Oxford University Press*, 1997.
2. M. Meot-Ner, *Chem. Rev.*, 2005, **105**, 213.
3. N. Agmon, *Chem. Phys. Lett.*, 2000, **319**, 247.
4. M. E. Tuckerman, D Marx and M. Parrinello, *Nature*, 2000, **417**, 925.
5. W. H. Robertson, E. G. Diken, A. Price, J-W Shin and M. A. Johnson, *Science*, 2003, **299**, 1367.
6. R. Ludwig, *Angew. Chem. Int. Ed.*, 2003, **42**, 258.
7. C. Chandhuri, Y-S Wang, J. C. Jiang, Y. T. Lee and H-C Chang, *Mol. Simul.*, 2001, **99**, 1161.
8. A. B. McCoy, X. Huang, S. Carter and J. M. Bowman, *J. Chem. Phys.*, 2005, **123**, 064317.
9. C. C. M. Samson and W. Klopper, *J. Mol. Struct.*, 2002, **586**, 201.
10. J. R. Roscioli, E. G. Diken, M. A. Johnson, S. Horvath and A. B. McCoy, *J. Phys. Chem. A*, 2006, **110**, 4943.
11. M. Morita and K. Takahashi, *Phys. Chem. Chem. Phys.*, 2013, **15**, 14973.
12. G. Gilli and P. Gilli, *J. Mol. Struct.*, 2000, **552**, 1.
13. M. Ceriotti, J. Cuny, M. Parrinello and D. E. Manolopoulos, *Proc. Natl. Acad. Sci. U.S.A.*, 2013, **110**, 15591.
14. X-Z. Li, B. Walker and A. Michaelides *Proc. Natl. Acad. Sci. U.S.A.*, 2011, **108**, 6369.
15. M. E. Tuckerman, D. Marx, L. M. Klein and M. Parrinello, *Science*, 1997, **275**, 817.
16. M. Tachikawa and M. Shiga, *J. Am. Chem. Soc.*, 2005, **127**, 11908.
17. K. Suzuki, M. Shiga and M. Tachikawa, *J. Chem. Phys.*, 2008, **129**, 144310.
18. Y. Kawashima, K. Suzuki and M. Tachikawa, *J. Phys. Chem. A*, 2013, **117**, 5205.
19. Y. Ogata, Y. Kawashima, K. Takahashi and M. Tachikawa, *Theo. Chem. Acc.*, 2015, **134**, 1587.
20. Y. Kawashima and M. Tachikawa, *J. Chem. Theo. Comput.*, 2014, **10**, 153.
21. R. P. Feynman. A. R. Hibbs, McGraw-Hill, New York, 1965.
22. R. P. Feynman, Benjamin, New York, 1972.
23. L. S. Schulman, Wiley, New York, 1981.
24. T. Hamashima, Y-C. Li, M. C. H. Wu, K. Mizuse, T. Kobayashi, A. Fujii and J-L. Kuo, *J. Phys. Chem.*, 2012, **117**, 101.

25. E. Kamarchik, and J. Bowman *J. Phys. Chem. letters*, 2013, **4**, 2964-2969.
26. K. Mackeprang, V. Hanninen, L. Halonen, and H. G. Kjaergaard, *J. Chem. Phys.*, 2015, **142**, 094304.
27. J. S. Mancini and J. M. Bowman, *Phys. Chem. Chem. Phys.* 2015, **17**, 6222-6226.
28. A. D. Becke, *Phys. Rev. A*, 1988, **38**, 3098.
29. C. Lee, W. Yang and R. G. Parr, *Phys. Rev. B*, 1988, **37**, 785.
30. O. Vahtras, J. Almlöf and M. W. Feyereisen, *Chem. Phys. Lett.*, 1993, **213**, 514 .
31. M. W. Feyereisen, G. Fitzgerald and A. Komornicki, *Chem. Phys. Lett.*, 1993, **208**, 359.
32. R. Ahlrichs, H. Bär, H. Häser, H. Horn and C. Kölmel, *Chem. Phys. Lett.*, 1989, **162**, 165.
33. G. J. Martyna, M. L. Klein and M. Tuckerman, *J. Chem. Phys.*, 1992, **97**, 2635.
34. M. J. Frisch, G. W. Trucks, H. B. Schlegel, G. E. Scuseria, M. A. Robb, J. R. Cheeseman, G. Scalmani, V. Barone, B. Mennucci, G. A. Petersson, H. Nakatsuji, M. Caricato, X. Li, H. P. Hratchian, A. F. Izmaylov, J. Bloino, G. Zheng, J. L. Sonnenberg, M. Hada, M. Ehara, K. Toyota, R. Fukuda, J. Hasegawa, M. Ishida, T. Nakajima, Y. Honda, O. Kitao, H. Nakai, T. Vreven, J. A. Montgomery, Jr. J. E. Peralta, F. Ogliaro, M. Bearpark, J. J. Heyd, E. Brothers, K. N. Kudin, V. N. Staroverov, R. Kobayashi, J. Normand, K. Raghavachari, A. Rendell, J. C. Burant, S. S. Iyengar, J. Tomasi, M. Cossi, N. Rega, J. M. Millam, M. Klene, J. E. Knox, J. B. Cross, V. Bakken, C. Adamo, J. Jaramillo, R. Gomperts, R. E. Stratmann, O. Yazyev, A. J. Austin, R. Cammi, C. Pomelli, J. W. Ochterski, R. L. Martin, K. Morokuma, V. G. Zakrzewski, G. A. Voth, P. Salvador, J. J. Dannenberg, S. Dapprich, A. D. Daniels, O. Farkas, J. B. Foresman, J. V. Ortiz, J. Cioslowski and D. J. Fox, *Gaussian 09, Revision A.02*, Gaussian, Inc., Wallingford CT, 2009.
35. M. Morita and K. Takahashi, *Phys. Chem. Chem. Phys.*, 2013 **15**, 114.
36. V. Barone, M. Biczysko, and J. Bloino, *Phys. Chem. Chem. Phys.*, 2014, **16**, 1759.
37. M. Daido, Y. Kawashima and M. Tachikawa, *J. Comp. Chem.*, 2013, **34**, 2403.
38. H. Flyvbjerg and H. G. Petersen, *J. Chem. Phys.*, 1989, **91**, 461.
39. J. M. Dieterich and B. Hartke *Phys. Chem. Chem. Phys.* 2015, **17**, 11958-11961.
40. K Mizuse and A Fujii, *J. Phys. Chem. A*, 2012, **116**, 4868-4877.
41. G. E. Douberly, A. M. Ricks, B. W. Ticknor, and M. A. Duncan, *J. Phys. Chem. A*, 2008, **112**, 950-959.
42. J. R. Roscioli, L. R. McCunn, M. A. Johnson, *Science*, 2007, **316**, 249.

Table 1: Relative energies with and without zero point energy (E_{ZPE}) corrections and structural parameters of stable conformations obtained from several levels of theory.

		RI-	RI-	MP2/6-	CCSD(T)/6-
		B3LYP/TZVP	MP2/TZVPP	311++G(3df,3pd)	311++G(3df,3pd)
Conformer I	E_{tot}	0.00	0.00	0.00	0.00
	$E_{tot}+E_{ZPE}$	0.00	0.00	0.00	-
Conformer II	E_{tot}	0.28	0.36	0.25	0.26
	$E_{tot}+E_{ZPE}$	0.11	0.27	0.04	-
Geometry of	R_{O1O3}	2.582	2.559	2.565	-
Conformer I	R_{O2O3}	2.565	2.551	2.554	-
	δ_{H1}	-0.509	-0.493	-0.507	-
	δ_{H3}	-0.478	-0.477	-0.485	-
	ϕ_1	13.1	16.2	14.6	-
	ϕ_2	114.5	124.8	114.9	-
	ϕ_3	120.6	134.3	121.8	-
	ϕ_4	-22.1	-24.8	-20.7	-
Geometry of	R_{O1O3}	2.574	2.554	2.559	-
Conformer II	R_{O2O3}	2.574	2.554	2.559	-
	δ_{H1}	-0.494	-0.484	-0.492	-
	δ_{H3}	-0.493	-0.481	-0.492	-
	ϕ_1	19.6	10.3	23.6	-
	ϕ_2	-19.7	-10.5	-23.6	-
	ϕ_3	0.0	-0.3	0.0	-
	ϕ_4	-22.6	-25.8	-21.6	-

Table 2: Average values and statistical errors of several internal coordinates obtained from quantum and classical simulations at 50 K, 100 K, and 150 K. Standard deviations of statistical values are also shown.

			$R_{\text{Free OH}}^{\text{Ave.}}$	$R_{\text{OO}}^{\text{Ave.}}$	R_{O3H5}	$\delta_{\text{H}}^{\text{Ave.}}$
50 K	Quantum	Average value	0.978(0)	2.574(1)	0.979(0)	-0.450(2)
		Standard deviation	0.065	0.076	0.065	0.207
	Classical	Average value	0.963(0)	2.583(1)	0.964(0)	-0.511(1)
		Standard deviation	0.009	0.038	0.008	0.063
100 K	Quantum	Average value	0.978(0)	2.576(2)	0.979(0)	-0.450(3)
		Standard deviation	0.065	0.077	0.065	0.207
	Classical	Average value	0.963(0)	2.582(1)	0.965(0)	-0.509(1)
		Standard deviation	0.013	0.052	0.013	0.082
150 K	Quantum	Average value	0.979(0)	2.577(3)	0.979(0)	-0.452(5)
		Standard deviation	0.065	0.080	0.065	0.212
	Classical	Average value	0.964(0)	2.588(1)	0.965(0)	-0.517(1)
		Standard deviation	0.016	0.065	0.016	0.103

Table 3: Populations of each conformer obtained from quantum and classical simulations at 50 K, 100 K, and 150 K. Populations obtained from static electronic structure calculations are also shown.

%		50 K	100 K	150 K
Conformer I	Quantum	49.0	45.7	41.7
	Classical	92.6	60.6	54.5
	Static	70.0	57.8	51.9
Conformer II	Quantum	12.0	26.1	29.8
	Classical	4.6	17.5	17.0
	Static	30.0	42.2	48.1
Conformer C_2	Quantum	39.0	28.2	28.5
	Classical	2.8	21.9	28.5
	Static	-	-	-

Table 4: Selected vibrational peak position, in cm^{-1} , and intensity, in km/mol , calculated for conformer I using MP2/6-311++G(3df,3pd) with harmonic approximation, normal mode 4D and normal mode 6D calculation. See Fig. 2 for the vibrational modes.

Assignment	Harmonic Approx.		NM4D		NM6D	
	Peak	Intensity	Peak	Intensity	Peak	Intensity
OO Sym Str	310	74			353	95
OO Asym Str	338	145			346	272
IHB Asym Bend	1708	21	1739	1382	1740	1403
IHB Sym Bend	1722	122	1659	379	1651	346
IHB Asym Str	2428	3455	1622	2014	1618	1856
IHB Sym Str	2632	1420	1979	1425	1958	1227
IHB Sym Str+OO str					2312	129
IHB Sym Str+OO str					2331	49
					2355	0
					2746	25
					2797	4
					2803	4
					2831	5
					2864	122
Overtone IHB Asym Str	4856	0	2872	363	2903	180
					2941	45
					3069	83
Overtone IHB Sym Str	5265	0	3109	242	3080	71
					3154	67

Figure

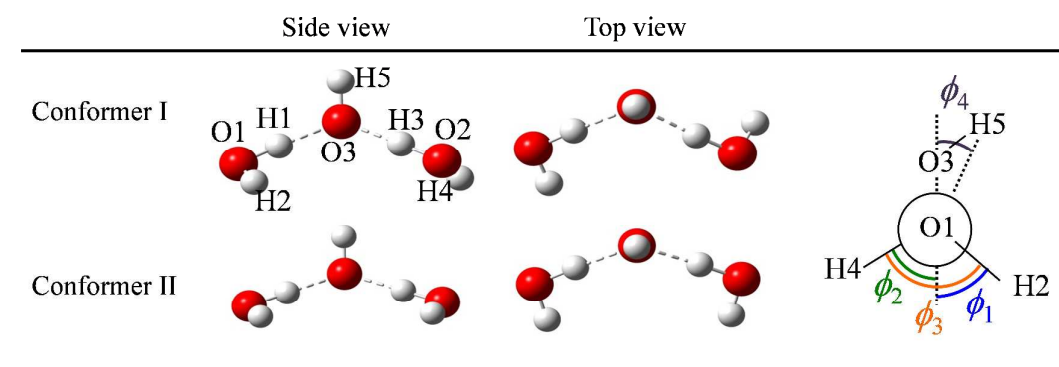


Figure 1: Schematic illustrations of stable conformers of $\text{OH}^-(\text{H}_2\text{O})_2$ and the schematic image of our dihedral angles defined by the Newman diagram along O1 and O2. The ϕ_1 , ϕ_2 , and ϕ_4 show the relative dihedral angles of H2, H4, and H5 atoms from the O1O3O2 plane, respectively. The ϕ_3 , which indicates the relative dihedral angle between H2 and H4 atoms, corresponds to the sum of ϕ_1 and ϕ_2 .

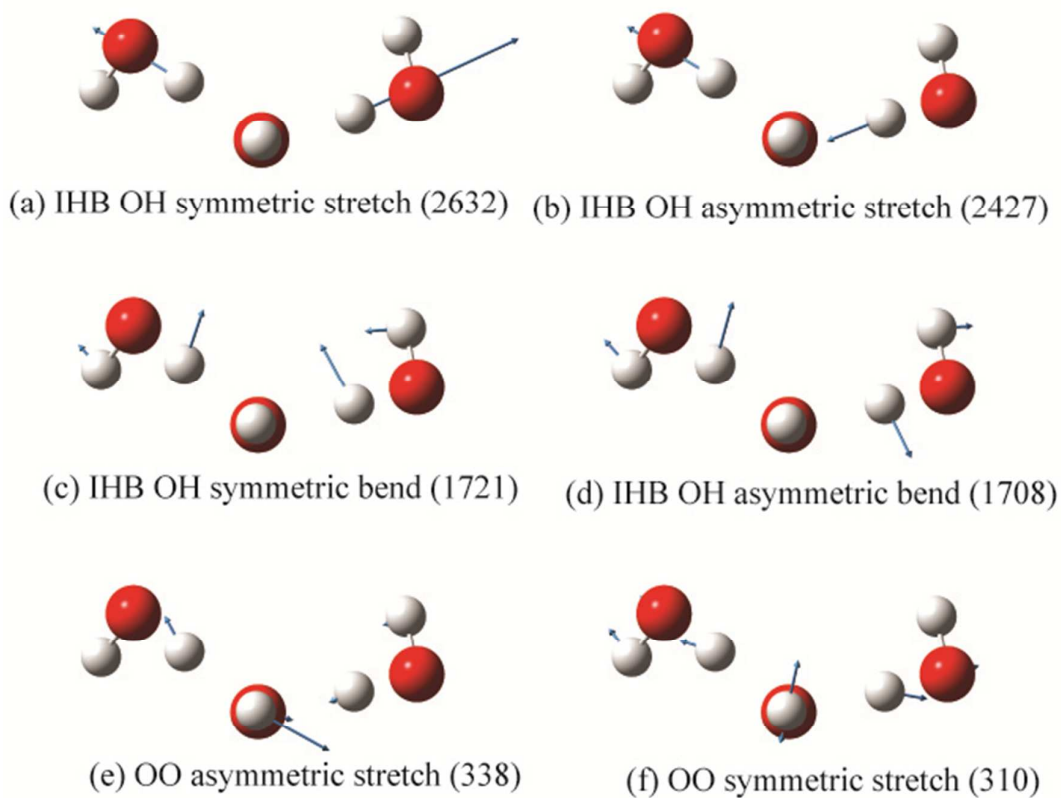


Figure 2: Schematic diagram of the IHB OH stretching, IHB bending, and VDW OO stretching vibration that are considered in the present study. The harmonic frequencies, in cm^{-1} , are given in parenthesis.

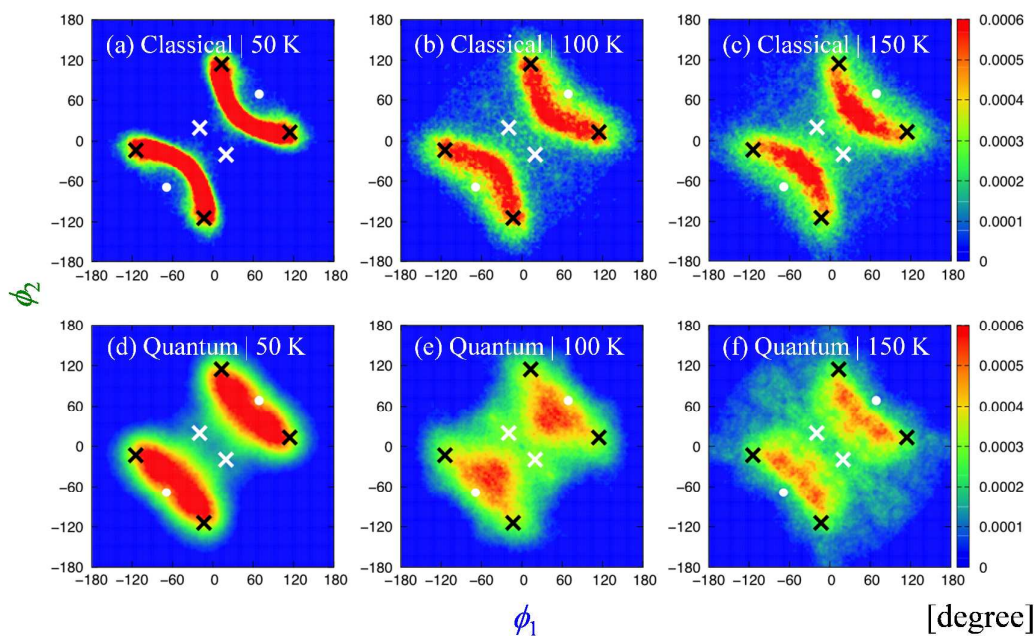


Figure 3: Two-dimensional distributions with respect to ϕ_1 and ϕ_2 for classical simulations at (a) 50 K, (b) 100 K, and (c) 150 K, and for quantum simulations at (d) 50 K, (e) 100 K, and (f) 150 K. Black and white crosses show the static values of Conformers I and II, respectively; while the white dot shows the static value of Conformer C₂.

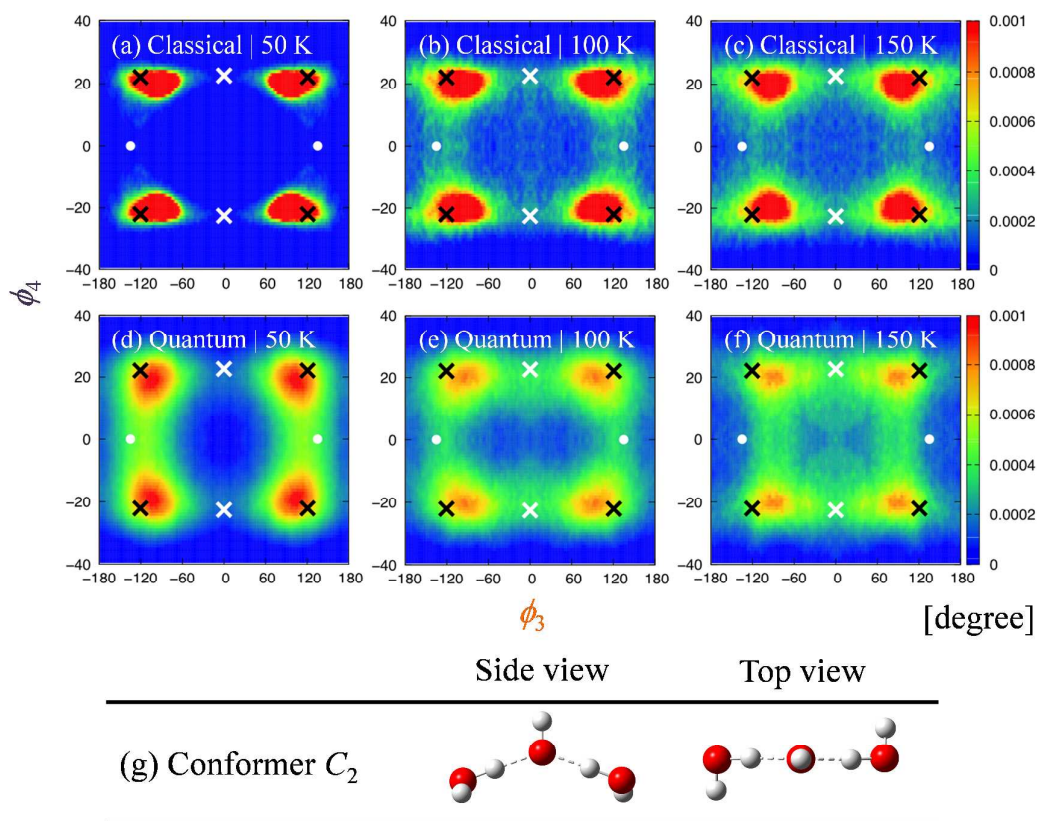


Figure 4: Two-dimensional distributions with respect to ϕ_3 and ϕ_4 for classical simulations at (a) 50 K, (b) 100 K, and (c) 150 K, and for quantum simulations at (d) 50 K, (e) 100 K, and (f) 150 K. Black and white crosses show the static values of Conformers I and II, respectively; while the white dot shows the static value of Conformer C_2 . Schematic illustrations for Conformer C_2 are also shown at (g).

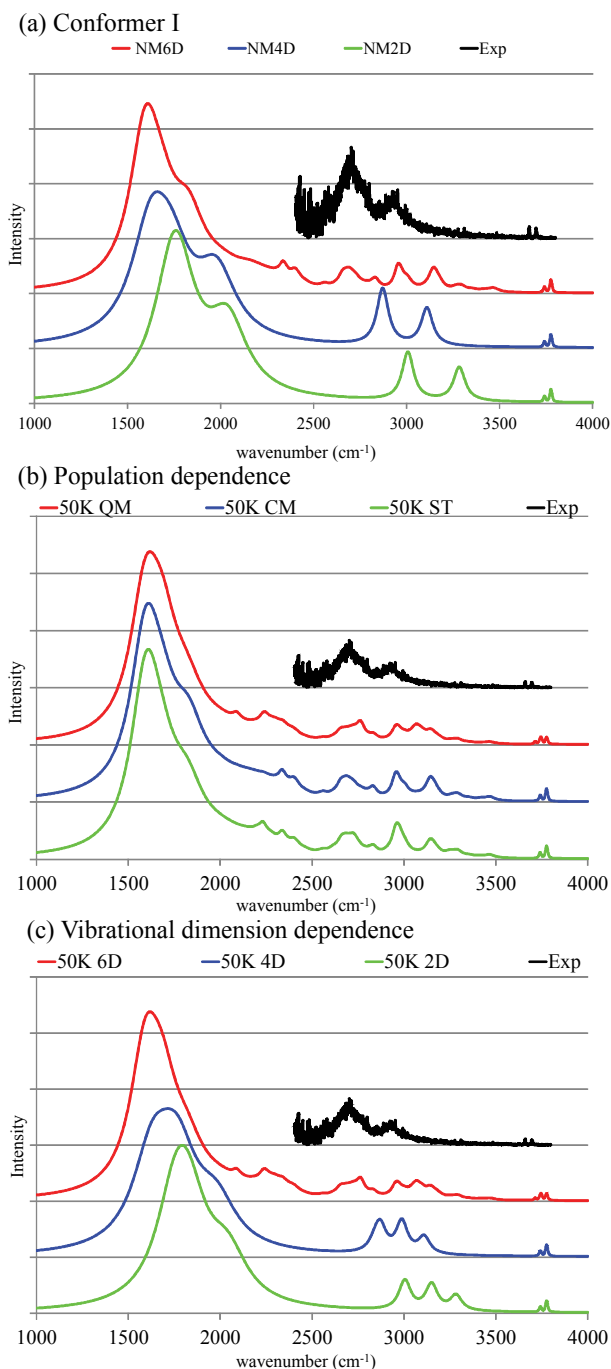


Figure 5: Theoretical vibrational spectra of (a) Conformer I, calculated by 2D, 4D, and 6D models are represented by green, blue, and red lines; and (b) 50 K spectra obtained using the 6D results along with the static, classical and quantum simulations are given by green, blue and red lines, respectively; and (c) spectra at 50 K obtained using the quantum population with the 2D, 4D, and 6D model are given by green, blue, and red lines, respectively.

Electronic Supplementary Material

Summary on the schematic diagram of the vibrational modes considered for the free OH and hydroxide stretching, schematic images of the processes of conformation change between Conformer I; the detailed analysis on the definition of the angles for each conformer; the details concerning the vibrational spectra; the 2D, 4D, and 6D vibrational spectra for conformers II and C_2 ; the temperature dependence of the vibrational spectra and the spectra calculated using the vibrational perturbation theory are all available in the electronic supplementary material.